

O(³P)+CO₂ scattering cross sections at superthermal collision energies for planetary aeronomy

Marko Gacesa,^{1,2*} R. J. Lillis,³ and K. J. Zahnle²

¹Bay Area Environmental Research Institute, Moffett Field, California, USA

²Space Science Division, NASA Ames Research Center, MS 245-3, Moffett Field, California, USA

³Space Sciences Laboratory, University of California, Berkeley, California, USA

Accepted XXX. Received YYY; in original form ZZZ

ABSTRACT

We report new elastic and inelastic cross sections for O(³P)+CO₂ scattering at collision energies from 0.03 to 5 eV, of major importance to O escape from Mars, Venus, and CO₂-rich atmospheres. The cross sections were calculated from first principles using three newly constructed ab-initio potential energy surfaces correlating to the lowest energy asymptote of the complex. The surfaces were restricted to a planar geometry with the CO₂ molecule assumed to be in linear configuration fixed at equilibrium. Quantum-mechanical coupled-channel formalism with a large basis set was used to compute state-to-state integral and differential cross sections for elastic and inelastic O(³P)+CO₂ scattering between all pairs of rotational states of CO₂ molecule. The elastic cross sections are 35% lower at 0.5 eV and more than 50% lower at 4+ eV than values commonly used in studies of processes in upper and middle planetary atmospheres of Mars, Earth, Venus, and CO₂-rich planets. Momentum transfer cross sections, of interest for energy transport, were found to be proportionally lower than predicted by mass-scaling.

Key words: scattering – molecular processes – planets and satellites: atmospheres – planets and satellites: terrestrial planets – planetary nebulae: general

1 INTRODUCTION

Understanding oxygen escape to space is a key to understanding evolution of the martian atmosphere. To first approximation, atomic hydrogen and oxygen escape from Mars are linked together. At present, H and O escape are directly related to water escape, as there is no pronounced evidence of excess of either species accumulating in the atmosphere. The global time-integrated rate of H escape is, therefore, equal to twice the global time-integrated O escape rate. While hydrogen escapes easily from Mars, mainly through thermal Jeans escape mechanism, atomic O escapes with difficulty due to its high mass (Hunten & Donahue 1976). As a result, it is the O escape rate that is limiting and its escape mechanism determines the loss of water and, consequently, plays the biggest role in determining the atmospheric evolution on Mars (Liu & Donahue 1976; Hunten & Donahue 1976; Lammer et al. 2003; Zahnle et al. 2008). Curiously, the same 2:1 ratio is inferred in H-to-O escape rates from Venus (Liu & Donahue 1975), suggesting principal importance of O escape at Venus, and for Venusian atmospheric evolution.

The mechanism driving the O escape from Mars is largely photochemical (Nagy & Cravens 1988; Jakosky et al. 2018). In its upper atmosphere, photodissociation of molecular O₂, O₃, CO₂, and CO by solar ultraviolet (UV) photons produces

superthermal atomic oxygen in the ground state, O(³P), as well as electronically excited O(¹D) and O(¹S). Dissociative recombination of O₂⁺ molecular ions with electrons preferentially produces superthermal O(³P), with kinetic energies up to 3.5 eV, capable of overcoming Mars' gravitational potential and escaping to space (Fox & Hać 2009). The photochemical escape appears to be the dominant non-thermal escape mechanism presently active on Mars (Lillis et al. 2017; Cravens et al. 2017).

Superthermal O atoms also drive escape of other atmospheric species, such as Ar, He, H₂, OH and H₂O, through kinetic energy transfer in collisions, contributing to additional non-thermal atmospheric loss (Leblanc et al. 2019). The non-thermal atmospheric escape rates strongly depend on the attenuation of the hot O flux in the Martian upper atmosphere, which mainly depends on O(³P)+CO₂ scattering properties at superthermal energies.

Owing to the fact that CO₂ is a greenhouse gas as well as an important coolant (via emission at 15 μm line) in the middle and upper atmosphere of Earth and terrestrial planets in general (Sharma & Wintersteiner 1990), the O(³P)+CO₂ scattering has been a subject of numerous investigations. Early theoretical work focused mainly on energy transfer to and from specific vibrational states (Bass 1974; Billing & Clary 1983; Schatz & Redmon 1981; Mullaney Harvey 1982; Garrett 1984). They found that the energy transfer could be described well using impulse approximation in the su-

* E-mail: marko.gacesa@nasa.gov

perthermal regime, similar to collisions of CO₂ with noble gas atoms (Suzukawa Jr et al. 1978). More recent studies covered the collision energies corresponding to temperatures 150 K $\leq T \leq$ 550 K, of interest in terrestrial atmosphere, and focused on understanding collisional de-excitation (quenching) of vibrationally excited CO₂ by the O atoms, namely O(³P)+CO₂(01¹0) \rightarrow O(³P) + CO₂(00⁰0), as well as energy transfer between internal rotational and vibrational degrees of freedom (Castle et al. 2006; de Lara-Castells et al. 2006, 2007; Castle et al. 2012; Feofilov et al. 2012; Cecchini & Castle 2015).

Yeung et al. (2012) experimentally and theoretically investigated O(³P)+CO₂ scattering at superthermal energies with isotopically labeled ¹²C¹⁸O₂. In a crossed molecular beam experiment at 4.28 eV (equal to 98.8 kcal/mol), they measured elastic and inelastic scattering of ¹⁶O(³P)+¹²C¹⁶O₂, as well as rate constants for two reactions: isotope exchange and O atom abstraction. They also performed quasi-classical trajectory (QCT) calculations for collision energies from 1 eV to 6.5 eV. However, the study of Yeung et al. (2012) was focused on understanding the role of transient molecular states in reactive scattering processes, in particular the oxygen isotope exchange and its role in atomic oxygen cycling via CO₂ in the Earth's atmosphere, rather than on constructing detailed elastic and inelastic scattering cross sections at superthermal energies for purposes of planetary aeronomy.

In the absence of targeted studies, in planetary aeronomy O(³P)+CO₂ scattering cross sections are commonly estimated by mass-scaling from systems whose scattering properties at superthermal energies are known better, including O+O (Kharchenko et al. 2000), O+N₂ (Balakrishnan et al. 1998), Ar+H₂ (Uudus et al. 2005), and O+H₂ (Gacesa & Kharchenko 2014), or from general properties of atom-molecule cross sections at high collision energies (Lewkow & Kharchenko 2014). For example, quantifying photochemical escape of oxygen from Mars (Cipriani et al. 2007; Fox & Hać 2009) and interpreting data from Mars Atmosphere and Volatile Evolution (MAVEN) mission (Lee et al. 2015b,a; Lillis et al. 2015, 2017; Leblanc et al. 2017; Amerstorfer et al. 2017) and collisionally-induced escape processes driven by superthermal O atoms (Bovino et al. 2011; Lammer 2013; Gacesa et al. 2012; Lewkow & Kharchenko 2014; Gacesa et al. 2017; Shematovich 2017), relied on mass-scaled cross sections specifically adapted for planetary aeronomy (Fox & Hać 2014, 2018). These studies recognized that accurate O(³P)+CO₂ cross sections are needed to reduced the uncertainties in present day atmospheric escape from Mars and estimates of its primordial water inventory (Lillis et al. 2017; Cravens et al. 2017; Jakosky et al. 2018).

Here, we present the results of a theoretical study of O(³P) + CO₂(*j*) \rightarrow O(³P) + CO₂(*j'*) elastic and inelastic quantum-mechanical scattering cross sections at collision energies between 0.03 and 5 eV. In addition, we present differential and momentum transfer cross sections, of interest for hot atomic oxygen transport and energy transfer at non-thermal-equilibrium conditions in middle and upper planetary atmospheres (Kao et al. 2019). Our newly constructed cross sections are of particular interest to Mars aeronomy missions, such as NASA's MAVEN mission (Jakosky et al. 2015) and ESA's Trace Gas Orbiter (TGO), as well as to future Venus missions (Kallio et al. 2011). Moreover, velocity-dependent O(³P) + CO₂(*j*) cross sections enter models seeking to ex-

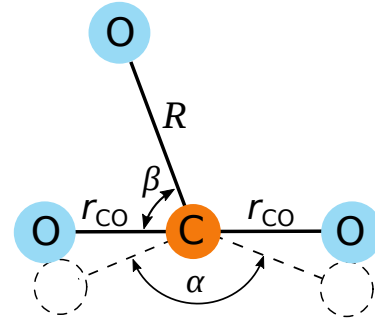


Figure 1. Coordinate system used to parameterize the potential energy surfaces of the O(³P)+CO₂ complex. Planar symmetry is assumed. The bending angle $\alpha = 180^\circ$ and $r_{\text{CO}} = 1.167 \text{ \AA}$ at equilibrium distance for a non-vibrating CO₂(00⁰0) molecule.

plain variations in the mass-independent fractionation (MIF) of stratospheric carbon dioxide (Thiemens et al. 1995; Wiegel et al. 2013) used to estimate carbon cycle reservoir size and rates of exchange for precise quantification of anthropogenic CO₂ and its effects on Earth's climate (Thiemens et al. 2014).

2 THEORETICAL METHODS

2.1 Electronic Structure of O(³P)-CO₂ complex

We first constructed *ab-initio* potential energy surfaces (PESs) for three energetically lowest electronic states of the CO₃ complex that correlate to the O(³P) asymptote. We assumed that the CO₂ molecule is in its ground vibrational state, CO₂(v_s, v'_b, v_a)=CO₂(00⁰0), where $v_s = 0$, $v'_b = 0$ and $v_a = 0$ are symmetric, bending, and asymmetric vibrational modes, respectively. Non-vibrating CO₂(00⁰0) is linear and symmetric, with the C-O internuclear distance, r_{CO} , fixed at the equilibrium potential obtained by geometry optimization (de Lara-Castells et al. 2006).

With this assumption, the rotational symmetry with respect to the OCO internuclear axis is preserved and the three PESs of the CO₃ complex can be described in 2D planar geometry in terms of distance R , defined as the internuclear distance between the impacting O(³P) atom and the C atom of the CO₂ molecule, and the angle $0^\circ \leq \beta \leq 90^\circ$ between the CO₂ internuclear axis and the vector R (Fig. 1). The symmetry group of the system will be at least C_s and depend on the angle of approach β . The lowest three PESs consist of a single ³A' and two ³A'' electronic states. The special cases when the symmetry of the system is increased are the T-approach ($\beta = 0^\circ$, symmetry group C_{2v}), and the colinear geometry ($\beta = 90^\circ$, symmetry group C_{∞v}) (see de Lara-Castells et al. (2007) for details).

We first evaluated the interaction energies of the complex at the spin-restricted single and double coupled-cluster with perturbative triple excitations (RCCSD(T)) level of theory (Knowles et al. 2000) with the frozen core approximation on the augmented correlation-consistent polarized triple zeta (aug-cc-pVTZ-DK) atomic basis (Dunning 1989; Kendall et al. 1992). We also carried out explicitly correlated calculations with partially spin-adapted scheme (RCCSD(T)-F12) (Knizia et al. 2009) on a cc-pVTZ-F12 basis set (Peterson et al. 2008). Explicitly correlated calculations pro-

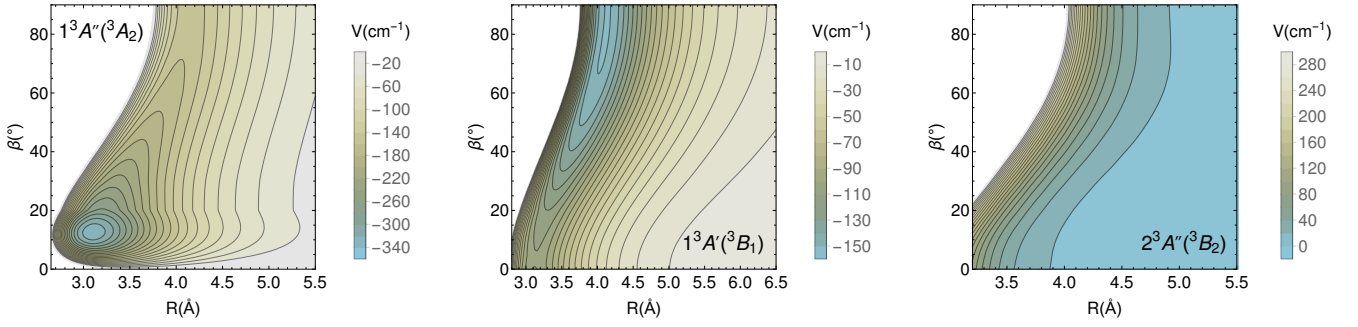


Figure 2. Contour plots of the three energetically-lowest potential energy surfaces for the $O(^3P)$ - CO_2 complex: $1^3A''$ (left), $^3A'$ (middle), $2^3A''$ (right). The CO_2 molecule is kept at equilibrium in linear geometry.

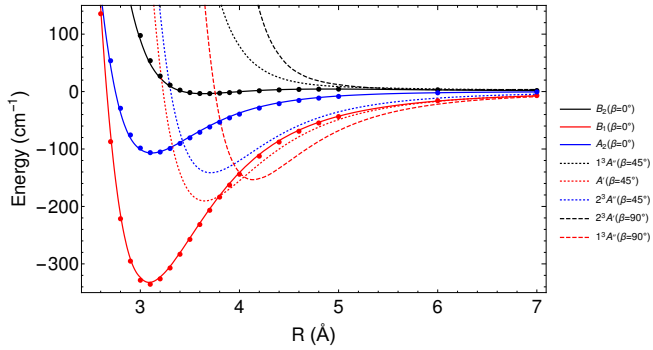


Figure 3. One-dimensional plots of the constructed $O(^3P)$ - CO_2 potential energy surfaces for the selected angles: $\beta = 0^\circ$ (T-approach; solid lines), $\beta = 45^\circ$ (dotted lines), and $\beta = 90^\circ$ (dashed lines). *Ab-initio* points of de Lara-Castells et al. (2006) for $\beta = 0^\circ$ are shown (filled circles) for comparison. CO_2 geometry is fixed as linear in equilibrium.

vide a dramatic improvement of the basis set convergence for coupled-cluster methods (Werner et al. 2010; Werner et al. 2011). Scalar relativistic effects for the system were observable and accounted for using the Douglas-Kroll-Hess Hamiltonian (Wolf et al. 2002). To construct primitive surfaces, we kept the C-O internuclear distances frozen at their optimized equilibrium values ($r_{CO} = 1.167 \text{ \AA}$) while varying the distance R , of the approaching O atom to the center of mass of the CO_2 molecule, on a non-equidistant grid with the highest point density around the global surface minima (if applicable). An equidistant grid in angle β with steps of 10° was used. A total of about 200 *ab-initio* points per surface were evaluated using both methods. All calculations were carried out using MOLPRO2012 (Werner et al. 2012a,b).

Final PESs were generated from the *ab-initio* points by constructing a fitting function of the form given by Sun et al. (2012) first proposed by Bukowski et al. (1999) (Fig. 2). We obtained excellent agreement with the PESs reported by de Lara-Castells et al. (2006) (Fig. 3), with differences per energy point $< 1\%$ on average. We note that a common coun-

terpoise technique (Boys & Bernardi 1970) to compensate for basis set superposition errors did not play a significant role, likely due to the large basis sets used and fast convergence of the explicitly correlated methods. A detailed report of our investigation of the electronic structure of CO_3 complex, including its dependence on the bending angles, falls out of the scope of the present work and will be published elsewhere.

2.2 Collisional Dynamics

We used MOLSCAT code (Hutson & Green 1994) to calculate state-to-state quantum mechanical elastic and inelastic cross sections for the scattering problem $O(^3P) + CO_2(j) \rightarrow O(^3P) + CO_2(j')$, where the j and j' are the initial and final rotational quantum numbers of the CO_2 molecule, respectively. The resulting set of time-independent coupled-channel Schrödinger equations was solved in close-coupling formalism with $CO_2(j)$ molecule represented as a rigid rotor with electronic interaction $O(^3P)$ described by our newly constructed potential energy surfaces (given in previous section). The complete scattering S -matrices, and differential and integral cross sections were calculated separately for each of the three triplet PESs and statistically averaged to obtain the final values.

We solved the scattering problem for 41 collision energy points on an equidistant grid between $E_{col} = 240 \text{ cm}^{-1}$ [$2.976 \times 10^{-2} \text{ eV}$] and $E_{col} = 40240 \text{ cm}^{-1}$ [4.9891 eV] in steps of 1000 cm^{-1} [0.124 eV]. The reduced mass $\mu \equiv \mu_{O,CO_2} = 11.73 \text{ amu}$ was used. Extensive testing was conducted to ensure the convergence with respect to the basis set size and numerical integration parameters. For the basis set consisting of rotational functions defined in terms of j_{max} , the maximum allowed rotational quantum number of CO_2 molecule, we found that satisfactory convergence of the elastic cross sections can be achieved with a basis set as small as $j_{max} = 30$. This remained true even when the centrifugal sudden (CS) approximation (McGuire & Kouri 1974) was invoked to reduce the calculation size by approximating the transitions between rotational states higher than $\Delta j = 2$ (JZCSMX=2). Nevertheless, in order to ensure convergence of inelastic cross

Table 1. Numerical integration parameters used in MOLSCAT production runs.

Parameter	Value
j_{\max}	100
J_{\max}	900
JZCSMX	8
RMIN (Å)	0.7
RMAX (Å)	30 ^a
RVFAC	1.3
STEPS	12

^aAutomatic scaling with J was used.

sections for initial rotational states j , present in the Maxwell-Boltzmann tail for the thermal upper atmosphere of Mars, we carried out production runs using a much larger basis set, with $j_{\max} = 100$ and JZCSMX=8. The convergence with respect to J , the total rotational quantum number of the complex, was achieved for $J_{\max} = 200 - 900$, where J_{\max} increases with collision energy.

Numerical integration was performed using modified log-derivative (Manolopoulos 1986) and hybrid modified log-derivative/Airy (LDA) (Alexander & Manolopoulos 1987) propagators. We found that satisfactory precision could be achieved using the faster LDA scheme, with Airy propagator set up to automatically detect integration region boundaries. The production run parameters are given in Table 1.

3 RESULTS AND ANALYSIS

3.1 Elastic and inelastic cross sections

For the three PESs, we calculated elastic and inelastic state-to-state cross sections, $\sigma_{j,j'}(E)$, for the $\text{O}(^3P) + \text{CO}_2(j) \rightarrow \text{O}(^3P) + \text{CO}_2(j')$ scattering, where rotational quantum numbers j and j' range from 0 to j_{\max} . The total scattering cross sections on a surface is given by

$$\sigma_j(E) = \sum_{j'} \sigma_{j,j'}(E), \quad (1)$$

where $j' = 0 \dots j_{\max}$. The cross sections are shown in Fig. 4 as a function of the collision energy, $E = 0.03 - 5$ eV in the center-of-mass frame of reference, as well as in Table 2 for selected collision energies and rotational states.

With the exception of the lowest energy point ($E = 0.0297$ eV), our elastic cross sections, $\sigma_{0,0}(E)$, are greater than estimated scattering cross sections of Yeung et al. (2012), who based their value on a Lennard-Jones interaction potential constructed on the lowest surface with parameters estimated from the experiment, but smaller than the elastic cross sections of Lewkow & Kharchenko (2014) and semi-empirical values by Fox & Hać (2014, 2018) used in numerous recent studies of Mars aeronomy. Specifically, at $E = 0.5$ eV and $E > 4$ eV, our elastic cross sections appear to be smaller by more than 25% and 50%, respectively, than reported in the above studies. Moreover, our total cross sections are about 25% larger than the elastic cross sections, suggesting that internal (rotational) degrees of freedom of CO_2 molecule are significantly populated in collisions.

The relative significance of inelastic excitations is illustrated in Fig. 5, where we show cross sections $\sigma_{j=0,j'}(E)$ as

a function of rotational quantum number j' for selected collision energies. Low-energy O atoms are 2-10 times more efficient at exciting low rotational states of CO_2 , but do not carry enough kinetic energy to excite high rotational states. This is consistent with general predictions of scattering theory where longer interaction times lead to more efficient energy transfer.

At collision energies smaller than about 0.5 eV, the rotational basis set is sufficiently large to fully capture the scattering dynamics (*i.e.*, the collision energies do not exceed the highest rotational energy included in the basis set), resulting in the cutoff in the rotational excitation spectrum. For example, at collision energy $E = 0.28$ eV, rotational states up to $j' \approx 78$ can be excited (Fig. 5).

For collision energies higher than about 0.5 eV, all rotational channels are collisionally populated and the approximate contributions from $j' > j_{\max}$ are included in $\sigma_{j,j_{\max}}(E)$. This approach allows us to estimate the uncertainties introduced by the finite basis size for $j_{\max} = 100$ used in the production runs to be smaller than 0.1%, and largely negligible for low rotational levels (*e.g.*, $j' = 0 - 5$). For high rotational levels (*e.g.*, $j' > 15 - 20$), the uncertainty increases with collision energy and can be estimated to about 1-2% for $j' > 20 - 40$ and up to 10% at $j' = 90 - 100$ at $E > 4$ eV.

3.2 Differential cross sections

State-to-state differential cross sections (DCSs) were calculated from the numerically evaluated scattering S -matrices over the considered collision energy range using the MOLSCAT utility code `dcssave.f`. The DCSs were constructed independently for each of the three PESs. The elastic DCSs, $Q_{j,j'}(\theta, E) = d\sigma_{j,j'}(\theta, E)/d\Omega$ and total DCSs, $Q_j(\theta, E) = \sum_{j'} d\sigma_{j,j'}(\theta, E)/d\Omega$, are illustrated in Fig. 6 for $j = 0$ in dependence on the center-of-mass collision energy E and the scattering angle θ . Here, $d\Omega = \sin\theta d\theta d\phi$ is the solid angle element and θ is the scattering angle, defined as the relative angle between the incoming and outgoing trajectories of the incoming $\text{O}(^3P)$ atom. In other words, $\theta = 0^\circ$ corresponds to complete forward scattering without deflection, $\theta = 90^\circ$ to sideways scattering, and $\theta = 180^\circ$ to complete backscattering. Example DCSs for two collision energies, 0.0297 eV and 2.5 eV, representative of low- and high-energy scattering, are given in Fig. 7

Both elastic and total DCSs are strongly anisotropic, with a dominant forward-scattering peak ($0^\circ < \theta < 2^\circ$ contributes to more than 90% of the integral cross section) and backscattering peaks clearly visible. Note that integral cross sections were calculated for the entire range of the scattering angle, $0^\circ < \theta < 180^\circ$. For small scattering angles θ , the DCSs are almost purely elastic. The inelastic excitations start to appear for $\theta > 3^\circ$ for low-energy collisions and for $\theta > 1^\circ$ for high-energy collisions (Fig. 7, inset). For larger scattering angles the total DCSs are up to two orders of magnitude greater than the elastic DCSs, suggesting that rotational excitations are dominant, in particular at higher collision energies. The oscillatory structure present in elastic cross sections, in particular at low collision energies, is a real feature that does not average out because the number of participating partial waves is much smaller than in case of total DCSs, where both elastic and inelastic channels are included. At higher collision energies the structure is smoothed out due to a much larger number of contributing partial waves. Note that the values

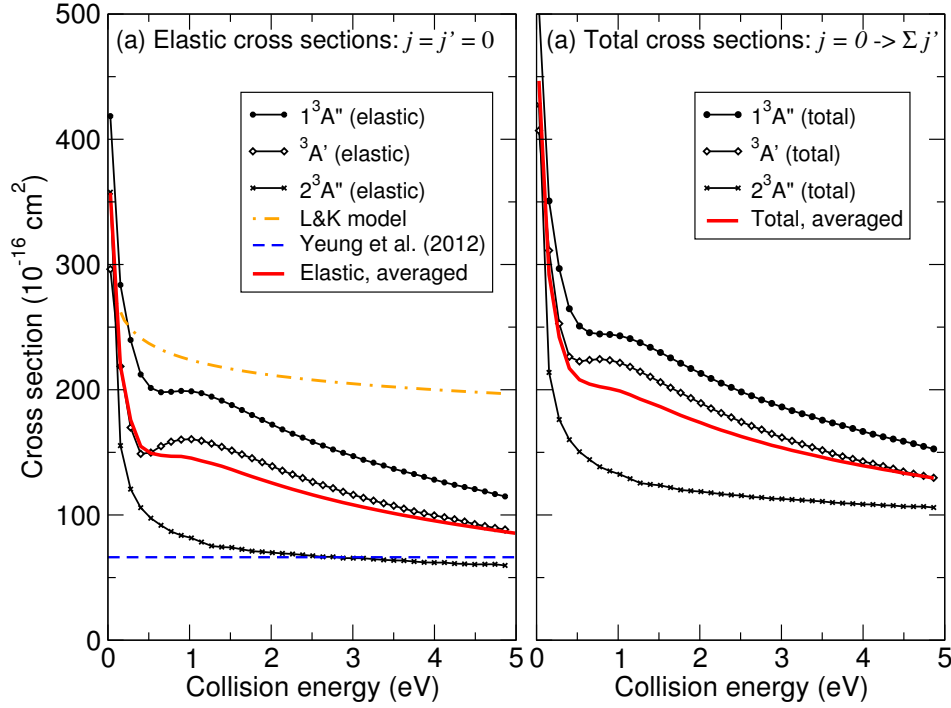


Figure 4. Cross sections for $O(^3P) + CO_2(j=0) \rightarrow O(^3P) + CO_2(j')$ scattering on three PESs: $1^3A''$ (circles), $3A'$ (diamonds), $2^3A''$ (crosses), and their statistically weighted average (solid line). *Left:* Elastic cross sections for $j=0$ compared to L&K model (Lewkow & Kharchenko 2014) (dot-dashed) and hard-sphere cross section (Yeung et al. 2012) (dashed). *Right:* Total (elastic + inelastic) cross sections $\sigma_{j=0}(E) = \sum_{j'} \sigma_{j'}(E)$, where $j' = 0$ to j_{max} .

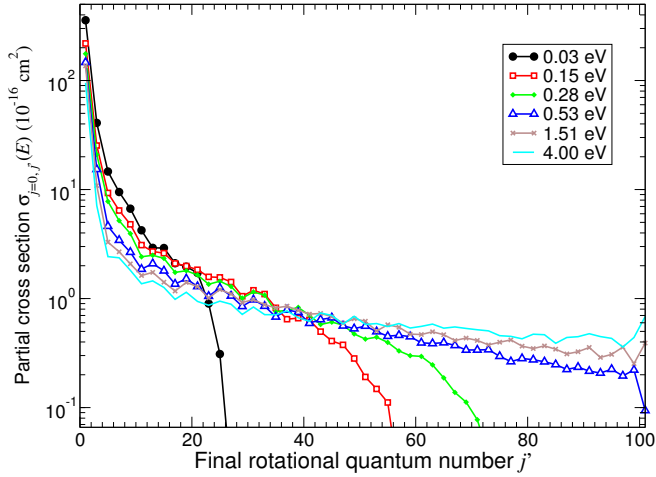


Figure 5. Cross sections $\sigma_{j=0,j'}(E)$ for $O(^3P) + CO_2(j=0) \rightarrow O(^3P) + CO_2(j')$ scattering on statistically averaged PES given as a function of j' for selected collision energies. Estimated uncertainties due to finite basis size are shown as residual values at $j' = 101$ (last point).

shown in Fig. 5 are for a single energy rather than averaged out over a realistic velocity distribution. At low collision energies several wave envelopes with maxima at scattering angles θ equal to about 30° , 70° , 100° , and 140° can be resolved. The complete dataset containing state-to-state CSs and DCSs is available online (Gacesa et al. 2019) as well as on request.

3.3 Momentum transfer cross section

Momentum transfer (or momentum *transport*) cross section (MTCS) is an effective quantity suitable for modeling the average momentum transferred from a projectile to the target particle in a binary collision. MTCSs are used in studies of energy exchange, diffusion, and transport in non-thermal environments in astrophysics, atmospheric science, and aeronomy (Kharchenko et al. 1997; Zhang et al. 2009).

For $O(^3P) + CO_2(j=0) \rightarrow O(^3P) + CO_2(j'=0)$ elastic scattering, the momentum transfer cross section is given by

$$\sigma_{j=0}^{mt}(E) = \int_0^\infty Q_{0,0}(\theta, E) \sin\theta(1 - \cos\theta) d\theta, \quad (2)$$

where $Q_{0,0}(\theta, E)$ is the differential cross section for $j = j' = 0$. Following Eq. (2), we have calculated MTCSs as a function of collision energy independently for each PES, as well as their statistically weighted average (Fig. 8).

Computed MTCSs are on average less than 1% of the elastic and total cross sections, except for low energy collisions, indicating that energy transfer from superthermal O to thermal CO_2 background is rather inefficient (Fig. 8, *inset*) even in comparison with $O(^3P)+H_2$ collisions where MTCSs are greater than 2% (Gacesa et al. 2012). In comparison, in the same collision energy range, MTCSs for atom-atom collisions tend to be about 10%-25% of the total cross sections between a heavy projectile and a light target species such as N+He, and about 2%-18% for heavy species, such as N+Ar (Zhang et al. 2008). The evaluated MTCSs have direct consequences on Mars aeronomy and atmospheric escape, where we can expect larger escape fluxes of non-thermal atomic oxygen produced at lower altitudes (Lillis et al. 2017), and possibly

Table 2. State-to-state cross sections $\sigma_{j=0,j'}(E)$ (units of 10^{-16} cm²) for selected energies.

j'	Center-of-mass collision energy E (eV)								
	0.0297	0.154	0.28	0.53	0.77	1.51	2.5	3.5	4.0
0	357.16	218.851	175.952	146.854	145.377	136.222	116.021	101.273	95.37
2	40.858	25.328	20.963	15.329	13.266	10.877	8.609	7.512	7.122
4	14.632	9.308	7.779	4.616	3.974	3.294	2.78	2.489	2.426
6	9.495	6.425	5.182	3.433	3.084	2.686	2.484	2.389	2.367
8	6.674	4.799	3.94	2.663	2.426	2.083	1.838	1.801	1.815
10	4.23	3.094	2.417	1.862	1.713	1.628	1.457	1.369	1.367
12	2.918	2.701	2.497	2.093	1.942	1.74	1.586	1.477	1.452
14	2.91	2.61	2.337	1.798	1.683	1.413	1.304	1.275	1.265
16	2.11	2.101	1.739	1.36	1.258	1.173	1.056	1.017	0.983
18	1.96	1.988	1.799	1.521	1.415	1.406	1.311	1.18	1.142
20	1.721	1.838	1.645	1.291	1.37	1.289	1.051	0.994	0.941
22	0.901	1.581	1.354	1.052	1.128	1.014	0.933	0.87	0.868
24	0.31	1.564	1.443	1.252	1.16	1.21	1.049	0.984	0.947
26		1.42	1.291	1.057	1.049	1.103	0.875	0.875	0.888
28		1.051	1.009	0.848	0.974	0.92	0.761	0.74	0.716
30		1.192	1.15	0.976	1.027	0.978	0.891	0.846	0.837
32		1.1	1.076	0.853	0.822	0.878	0.785	0.736	0.712
34		0.823	0.759	0.679	0.739	0.822	0.69	0.707	0.71
36		0.647	0.78	0.788	0.918	0.852	0.818	0.812	0.772
38		0.661	0.83	0.75	0.786	0.781	0.7	0.646	0.667
40		0.636	0.702	0.594	0.613	0.72	0.668	0.627	0.618
42		0.497	0.578	0.642	0.728	0.73	0.749	0.728	0.737
44		0.408	0.608	0.668	0.702	0.684	0.793	0.692	0.701
46		0.376	0.572	0.563	0.541	0.596	0.633	0.583	0.584
48		0.282	0.474	0.53	0.557	0.653	0.687	0.681	0.688
50		0.191	0.425	0.56	0.595	0.62	0.662	0.609	0.579
52		0.148	0.443	0.498	0.511	0.504	0.594	0.579	0.59
54		0.111	0.396	0.452	0.494	0.575	0.65	0.608	0.554
56			0.331	0.462	0.496	0.546	0.619	0.603	0.589
58			0.299	0.448	0.465	0.472	0.557	0.575	0.537
60			0.295	0.393	0.432	0.468	0.557	0.591	0.556
62			0.247	0.387	0.447	0.496	0.569	0.579	0.583
64			0.187	0.394	0.411	0.466	0.474	0.522	0.535
66			0.138	0.372	0.39	0.413	0.466	0.528	0.549
68			0.112	0.338	0.385	0.434	0.48	0.515	0.532
70			0.077	0.338	0.376	0.413	0.498	0.537	0.517
72			0.036	0.34	0.356	0.376	0.444	0.468	0.506
74			0.008	0.296	0.334	0.398	0.456	0.456	0.456
76				0.264	0.317	0.418	0.429	0.447	0.45
78				0.282	0.324	0.366	0.405	0.424	0.427
80				0.275	0.332	0.348	0.407	0.442	0.471
82				0.263	0.293	0.368	0.416	0.476	0.466
84				0.248	0.273	0.343	0.392	0.394	0.389
86				0.224	0.285	0.31	0.411	0.426	0.44
88				0.235	0.276	0.326	0.422	0.427	0.447
90				0.216	0.251	0.356	0.359	0.421	0.476
92				0.208	0.268	0.289	0.372	0.47	0.448
94				0.225	0.249	0.308	0.447	0.434	0.432
96				0.195	0.272	0.359	0.346	0.357	0.359
98				0.221	0.269	0.253	0.328	0.413	0.44
100 ^a				0.094	0.215	0.391	0.569	0.669	0.685

^aContributions from all $j' > 100$.

other atomic species, such as C and N, escaping through a thick layer of CO₂.

4 SUMMARY AND DISCUSSION

We have carried out a theoretical study of O(³P) + CO₂ → O(³P) + CO₂ non-reactive scattering at thermal and su-

perthermal collision energies up to 5 eV in the center-of-mass frame. The selected energy range is typical in non-thermal-equilibrium conditions in upper planetary atmospheres exposed to solar radiation and plasma inputs. To describe the electronic interactions between the colliding particles, we have constructed *ab-initio* potential energy surfaces for three electronic states correlating to the energetically-lowest

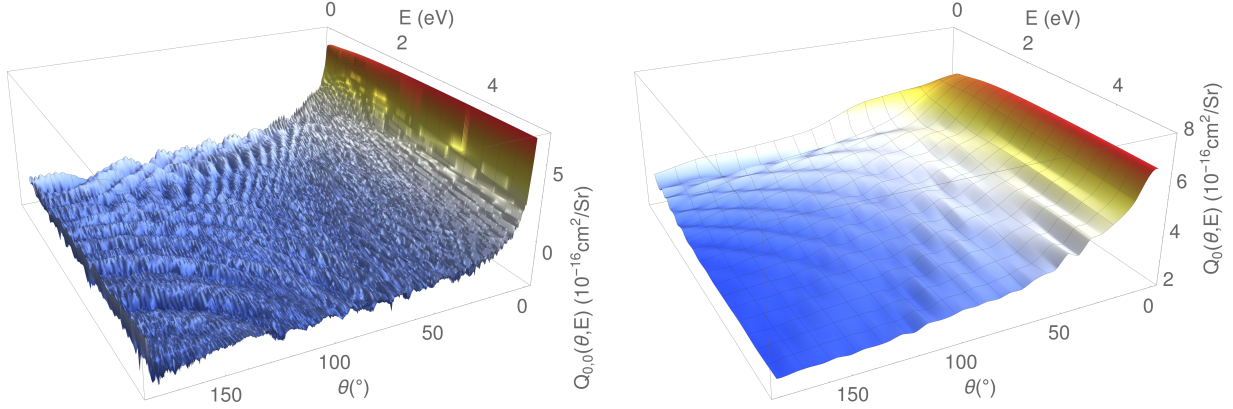


Figure 6. Elastic (left panel) and total (right panel) differential cross sections for $O(^3P) + CO_2(j=0)$ scattering, statistically averaged over all PESs and presented in log scale.

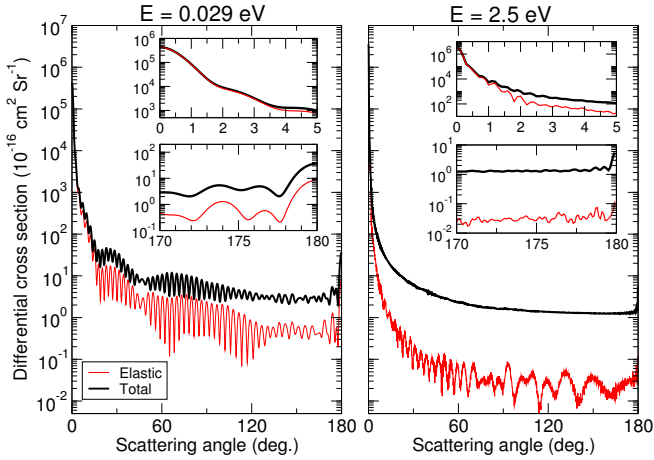


Figure 7. Elastic (thin red line) and total (thick black line) DCSs as functions of scattering angle shown for collision energies $E=0.0297$ eV (left panel) and $E=2.5$ eV (right panel). *Insets:* Zoom in on small (top) and large (bottom) scattering angles.

asymptote of the $O(^3P)-CO_2(^1\Sigma^+)$ complex. The surfaces were constructed in a restricted planar geometry, with the CO_2 molecule assumed to be linear with C-O internuclear separation fixed at the equilibrium distance.

With the PESs as inputs, we computed velocity-dependent state-to-state and total elastic and inelastic cross sections, corresponding differential cross sections, as well as elastic momentum transfer cross sections. The CO_2 molecule was modeled as a rigid rotor and rotational-vibrational couplings between the symmetric, bending, and asymmetric vibrational modes were not included in the production run of the model. The scattering problem was described using a quantum mechanical coupled-channel formalism and solved numerically.

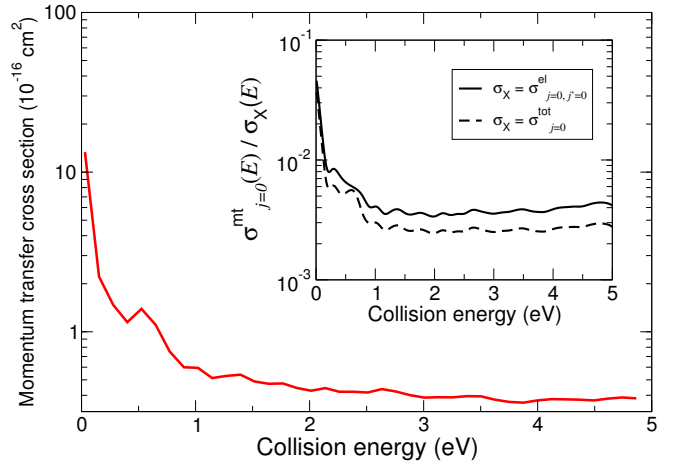


Figure 8. Momentum transfer cross section $\sigma_{j=0}^{mt}(E)$ for $O(^3P) + CO_2(j=0)$ as a function of collision energy statistically averaged over three PESs. *Inset:* Ratio of the MTCS and elastic and total cross sections, respectively, for the same initial state.

Thus, the cross sections and derived physical quantities were constructed from first principles without any external empirical parameters. Although computationally intensive, the *ab initio* approach has several major advantages over classical theory, such as evaluation of all state-to-state transitions induced by collisions and more complete treatment of purely quantum effects, expected to play a significant role in improving the predictive power and precisions of models (Kao et al. 2019).

Our computed elastic cross sections are smaller than the elastic cross sections estimated by mass-scaling from well-described atom-molecule systems (Lewkow & Kharchenko 2014; Fox & Hać 2018), but larger than the Lennard-Jones

cross section reported by [Yeung et al. \(2012\)](#). Specifically, at superthermal energies, our elastic cross sections range between 1.5×10^{-14} cm² at about 1 eV collision energy, down to 8.5×10^{-15} cm² at 5 eV. In comparison, the widely used elastic cross sections of [Lewkow & Kharchenko \(2014\)](#) evaluate to 2.24×10^{-14} cm² and 1.97×10^{-14} cm² for the two collision energies, respectively. Calculated differential cross sections (DCSs) are strongly favoring forward scattering with the anisotropy increasing with the collision energy. The small-angle forward scattering is mostly elastic with negligible kinetic energy transfer to internal degrees of freedom of the CO₂ molecule. In contrast, for larger scattering angles the inelastic DCSs are nearly two orders of magnitude greater than elastic ones, indicating that the kinetic energy transfer to internal excitations is rather efficient. For the highest collision energies considered, the total inelastic CS is equal to approximately one half of the elastic CS, suggesting that up to 50% of the translational kinetic energy of the O(³P) atom is converted into internal excitations (rotations) of the CO₂ molecule. [Yeung et al. \(2012\)](#) observed significant energy transfer in the O(³P) + CO₂ system, with “an average of only 41% of the collision energy remaining in product translation”. A simple statistical estimate based on level energies puts that number as high as 75% ([Fox & Hać 2018](#)). In comparison, in O(³P)+CO collisions, on average 84% of the energy remains in product translation, approximately 80% is retained in Ar + ethane collisions, and 60% in superthermal O(³P)+C₂H₆ collisions. [Yeung et al. \(2012\)](#) suggested that such a large fraction of kinetic energy transfer to inelastic excitations may be due to significant contribution from a short-lived intermediate CO₃ complex that can form in the collisions and yield reaction products corresponding to inelastic scattering of O(³P)+CO₂.

The most significant contribution to the uncertainties in the calculated cross sections comes from approximating the CO₂ molecule with a linear rigid rotor. With vibrational modes and rotational-vibrational coupling included in the model, we expect our inelastic (and total) scattering cross sections to be lower than what nature intended because of absence of direct kinetic energy transfer into vibrational modes. The effects should be more significant at the high-end of the collision energy range considered, above about 4 eV, where the vibrational excitations were predicted to overtake rotational excitations as a dominant inelastic process ([Schatz & Redmon 1981](#)).

Based on energy transfer arguments and reported vibrational cross sections in existing studies, we can attempt to estimate the uncertainties of our results. If we require 65% of translational energy to be converted into internal excitations of CO₂ molecule at collision energy $E = 4.3$ eV, as proposed by [Yeung et al. \(2012\)](#), our total cross sections should be increased by about 13%, to $\sigma_{j=0} \approx 1.5 \times 10^{-14}$ cm². Similarly, at lower collision energies, our total cross sections should be increased by a proportionally smaller percentage, as per energy arguments. Note that the estimated fraction of the translational energy transferred to the internal excitations by [Yeung et al. \(2012\)](#) is rather high.

In comparison, a theoretical study of vibrational excitations in the title process based on the infinite-order-sudden (IOS) approximation ([Mullaney Harvey 1982](#)) reported cross sections for collisionally exciting CO₂(01¹0) (first bending mode) greater than 5.6×10^{-17} cm² at $E > 2$ eV, or less

than 1% of our elastic cross sections. [Upschulte & Caledonia \(1992\)](#) measured the cross sections for O-atom excitation of CO₂(00⁰1) mode at $E = 3.9$ eV (8 km/s) to be equal to 3.7×10^{-18} cm² and recommended a value of 6.4×10^{-17} cm² as a cross section for O-atom excitation of CO₂(01¹0). Their proposed values are in good agreement with a quasi-classical trajectory (QCT) study of collisional excitation of CO₂(NN' 1), where N and N' correspond to excited symmetric and bending vibrational modes, respectively ([Schatz & Redmon 1981](#)). These studies suggest that the cross sections for collisional excitation of the lowest antisymmetric vibrational mode of CO₂ are, at best, nearly two orders of magnitude smaller than our inelastic (rotational) cross sections. If we assume that the total inelastic cross section for vibrational excitations scales linearly with the number of open channels (vibrational states), we can make a more direct comparison with our results. At collision energy $E = 3.9$ eV, lowest 14 antisymmetric vibrational modes, up to $v_a = 13$, can be excited, yielding a total vibrational cross section 8.3×10^{-16} cm² for CO₂(NN' , 13), or about one half of the value estimated from the translational energy fractions.

The elastic cross sections are less likely to be significantly affected by the absence of vibrational excitations in our model. We tested the convergence of scattering calculations for basis sets comprised of as few as six internal states ($J'_{\max} = 5$), or of only 5-10 bending mode energies ($E_b = 667$ cm⁻¹) with rotational states modeled using the IOS approximation ([Goldflam et al. 1977](#); [Green 1979](#)). The elastic cross sections computed with these minimal basis sets were about 20% larger than our production values, while a basis set with as few as 30 rotational states matched the production values within 2%. Nevertheless, matching the production inelastic cross sections required large basis sets.

Three final points should be mentioned. First, deviation from the linear geometry (bending angle $\alpha \neq 180^\circ$) will likely have an effect on the cross sections. [de Lara-Castells et al. \(2006, 2007\)](#) constructed PESs for the bending angles $150^\circ < \alpha < 210^\circ$ and demonstrated that for $\alpha < 180^\circ$, for which the CO₂ molecule bends towards the incoming O(³P) atom, the surfaces become more attractive and have deeper wells, while the opposite is true for $\alpha > 180^\circ$. However, since the binding angle is directly connected to the strength of rotational-vibrational couplings, it is difficult to assess the effects of geometry changes without conducting further studies with vibrational degrees of freedom included in the model. Our preliminary calculations match well the PESs of [de Lara-Castells et al. \(2006\)](#) for bending angles $150^\circ < \alpha < 210^\circ$ and the work to extend the scattering model to include vibrations is in progress. Second, even though we conducted the scattering calculations on three PESs correlating to the lowest energy asymptote of O(³P) + CO₂ complex, we did not take into account intersurface couplings that could lead to surface hopping. Such studies were conducted for spin-orbit couplings at lower collision energies ([de Lara-Castells et al. 2007](#)) and the impact of surface hopping on cross sections at similar scattering energies were analyzed for other atom-molecule systems ([Maiti & Schatz 2003](#); [Li & Han 2009](#); [Gacesa & Kharchenko 2014](#)). Based on these studies, we estimate that for high collision energies considered in this study at current level of theory, the intersystem crossing effects are not likely to significantly affect the final results. Third, we note that reactive processes were not considered in this study. [Yeung](#)

et al. (2012) calculated the branching fractions for nonreactive scattering to be 0.984, as compared to the oxygen-atom abstraction reaction (4×10^{-6}) and O atom exchange (0.016), with the uncertainties of about 30% cited for all processes. Thus, we estimate that neglecting nonreactive channels contributes to no more than 2% uncertainties in the reported cross sections.

4.1 Implications on planetary aeronomy and escape of hot oxygen from Mars

Current estimates of photochemical oxygen escape rates at Mars vary between about 10^{24} s^{-1} to 10^{26} s^{-1} . While the numerical methods used between the studies are different (commonly Monte Carlo simulations vs two-stream solutions), O+CO₂ cross sections were identified as the key quantity responsible for the O escape rate variations (Cravens et al. 2017; Jakosky et al. 2018).

The O(³P)+CO₂ cross sections computed in this work are between 30% and 50% smaller than the values obtained by mass-scaling or semi-empirical methods that have been commonly used in interpretations of Mars orbiter data and simulations of photochemical oxygen escape(). Specifically, our elastic cross sections are about $1.5 \times 10^{-14} \text{ cm}^2$ at 1 eV collision energy and about $8.5 \times 10^{-15} \text{ cm}^2$ at 5 eV. In comparison, the widely used elastic cross sections of Lewkow & Kharchenko (2014) evaluate to $2.24 \times 10^{-14} \text{ cm}^2$ and $1.97 \times 10^{-14} \text{ cm}^2$ for the two collision energies, respectively. In addition, the cross sections obtained by mass-scaling themselves scale with collision energy in the same way as the system on which they were based (typically O-O cross sections constructed for energy transfer in the terrestrial atmosphere by Kharchenko et al. (2000)), or are assumed constant over the entire collision energy range (). Similar arguments extend to differential cross sections: they either resemble the original system, or do not include angular anisotropy.

We can estimate the impact of newly computed cross sections presented here on the hot oxygen escape flux at Mars. Cravens et al. (2017) recently constructed a simple but robust analytic model of hot oxygen escape from Mars that scales well over a large range of solar EUV irradiances. Under the assumptions from their model, the photochemical oxygen escape flux from Mars is given by

$$F_{\text{esc,O}} \approx 0.1 \times I_{\text{CO}_2}(1 \text{ AU}) / \sigma_{\text{O-CO}_2}^{\text{back}}, \quad (3)$$

where $I_{\text{CO}_2}(1 \text{ AU})$ is the photoionization frequency for CO₂ at 1 AU distance from the Sun and $\sigma_{\text{O-CO}_2}^{\text{back}}$ is the total backscattering cross section for O+CO₂ collisions. Global escape rate can be approximated as $Q_{\text{esc}} = 2\pi R_{\text{Mars}} F_{\text{esc,O}}$, where it is assumed that the escape takes place from an ideal hemisphere under solar illumination.

In Table 3 we compare global O escape rates calculated using the total backscattering cross sections at 2.5 eV and 3.5 eV constructed in this paper (see Fig. 7) with representative values given in the literature. A more complete list of estimated O escape rates with references can be found in Cravens et al. (2017). The solar activity (irradiance) index $F_{10.7}$ is used to define solar maximum ($F_{10.7} = 200$), minimum ($F_{10.7} = 70$), and moderate activity ($F_{10.7} = 130$).

Our estimated photochemical O escape rates are larger than in Cravens et al. (2017) by about a factor of two and significantly larger than Fox & Hać (2018) for all levels of

Table 3. Global Photochemical Oxygen Escape Rates at Mars.

$Q_{\text{esc}} [\text{s}^{-1}]^a$	Collision energy		Literature ^c		
	2.5 eV	3.5 eV	C17	L17	FH18
solar maximum	20 ^a	16	9		4
solar minimum	7	5	3		0.7
solar moderate	13	10	6	4.3	
$\sigma_{\text{O-CO}_2}^{\text{back}} [10^{-16} \text{ cm}^2]$	6.27	8.05	13		

^a Q_{esc} in units of 10^{25} s^{-1} .

^cC17=Cravens et al. (2017), L17=Lillis et al. (2017), FH18=Fox & Hać (2018).

solar activity, with the differences being greater at 2.5 eV than at 3.5 eV. Consequently, we can expect photochemical hot O escape rates from Mars estimated using mass-scaling O+CO₂ cross sections would be up to two times greater if the cross sections presented in this work would be used instead. For example, we estimate that the escape rates constructed by Cravens et al. (2017) would increase to $\approx 8.5 \times 10^{25} \text{ s}^{-1}$. In comparison, the hot O escape rates derived from MAVEN observations of H⁺ and O⁺ ions picked up by the solar wind (i.e., pickup ions) have a mean value of $9 \times 10^{25} \text{ s}^{-1}$ with a factor of two variability (Rahmati et al. 2018). Thus, a significantly better agreement between the two rates derived from measurements performed using different instruments onboard MAVEN orbiter could be reached if the cross sections presented here were used to model O+CO₂ collisions and their impact on attenuation of the hot O escape flux.

ACKNOWLEDGEMENTS

MG and KZ have been partially funded by NASA, grant #17-MDAP17-2-0152. The authors are grateful to J. Fox, Y. Lee, and B. Jakosky for helpful suggestions and discussion, and to M.-P. de Lara-Castells for sharing with us a digital version of their potential energy surface points. An expert reviewer is acknowledged for providing helpful comments and suggestions that improved the quality of the article.

REFERENCES

- Alexander M. H., Manolopoulos D. E., 1987, *Journal of Chemical Physics*, 86, 2044
- Amerstorfer U. V., et al., 2017, *Journal of Geophysical Research: Planets*, 122, 1321
- Balakrishnan N., Kharchenko V., Dalgarno A., 1998, *J. Geophys. Res.*, 1032, 23393
- Bass J. N., 1974, *J. Chem. Phys.*, 60, 2913
- Billing G. D., Clary D. C., 1983, *Chemical Physics*, 80, 213
- Bovino S., Zhang P., Gianturco F. A., Dalgarno A., Kharchenko V., 2011, *Geophysical Research Letters*, 38, L02203
- Boys S. F., Bernardi F., 1970, *Molecular Physics*, 19, 553
- Bukowski R., Sadlej J., Jeziorski B., Jankowski P., Szalewicz K., Kucharski S. A., Williams H. L., Rice B. M., 1999, *J. Chem. Phys.*, 110, 3785
- Castle K. J., Kleissas K. M., Rhinehart J. M., Hwang E. S., Dodd J. A., 2006, *Journal of Geophysical Research: Space Physics*, 111, A09303
- Castle K. J., Black L. A., Simone M. W., Dodd J. A., 2012, *Journal of Geophysical Research: Space Physics*, 117, A04310

- Cecchini M. R., Castle K. J., 2015, *Chemical Physics Letters*, **638**, 149
- Cipriani F., Leblanc F., Berthelier J. J., 2007, *Journal of Geophysical Research: Planets*, **112**, E07001
- Cravens T. E., et al., 2017, *Journal of Geophysical Research: Space Physics*, **122**, 1102
- Dunning Jr. T. H., 1989, *J. Chem. Phys.*, **90**, 1007
- Feofilov A. G., Kutepov A. A., She C.-Y., Smith A. K., Pessnell W. D., Goldberger R. A., 2012, *Atmospheric Chemistry & Physics*, **12**, 9013
- Fox J. L., Hać A. B., 2009, *Icarus*, **204**, 527
- Fox J. L., Hać A. B., 2014, *Icarus*, **228**, 375
- Fox J. L., Hać A. B., 2018, *Icarus*, **300**, 411
- Gacesa M., Kharchenko V., 2014, *J. Chem. Phys.*, **141**, 164324
- Gacesa M., Zhang P., Kharchenko V., 2012, *Geophysical Research Letters*, **39**, L10203
- Gacesa M., Lewkow N., Kharchenko V., 2017, *Icarus*, **284**, 90
- Gacesa M., Lillis R. J., Zahnle K. J., 2019, O(3P)+CO₂ scattering cross sections at superthermal collision energies for planetary aeronomy: Raw data pre-release (v0.9-beta), [doi:10.5281/zenodo.3256699](https://doi.org/10.5281/zenodo.3256699), <https://doi.org/10.5281/zenodo.3256699>
- Garrett B. C., 1984, *Chemical Physics*, **87**, 63
- Goldflam R., Green S., Kouri D., 1977, *J. Chem. Phys.*, **67**, 4149
- Green S., 1979, *J. Chem. Phys.*, **70**, 4686
- Hunten D. M., Donahue T. M., 1976, *Annual Review of Earth and Planetary Sciences*, **4**, 265
- Hutson J. M., Green S., 1994, MOLSCAT Version 14, Collaborative Computational Project 6 (Daresbury Laboratory: UK Engineering and Phys. Sci. Res. Council), <http://www.giss.nasa.gov/tools/molscat/>
- Jakosky B. M., et al., 2015, *Space Sci. Rev.*, **195**, 3
- Jakosky B. M., et al., 2018, *Icarus*, **315**, 146
- Kallio E., Chaufray J.-Y., Modolo R., Snowden D., Winglee R., 2011, *Space Sci. Rev.*, **162**, 267
- Kao D.-Y., et al., 2019, in *Bulletin of the American Astronomical Society*. p. 240 ([arXiv:1904.07161](https://arxiv.org/abs/1904.07161))
- Kendall R. A., Dunning Jr. T. H., Harrison R. J., 1992, *J. Chem. Phys.*, **96**, 6796
- Kharchenko V., Tharamel J., Dalgarno A., 1997, *J. Atmospheric Sol.-Terr. Phys.*, **59**
- Kharchenko V., Dalgarno A., Zygelman B., Yee J.-H., 2000, *J. Geophys. Res.*, **105**, 24899
- Knizia G., Adler T. B., Werner H.-J., 2009, *J. Chem. Phys.*, **130**, 054104
- Knowles P. J., Hampel C., Werner H.-J., 2000, *J. Chem. Phys.*, **112**, 3106
- Lammer H., 2013, *Origin and Evolution of Planetary Atmospheres*, [doi:10.1007/978-3-642-32087-3](https://doi.org/10.1007/978-3-642-32087-3).
- Lammer H., Kolb C., Penz T., Amerstorfer U. V., Biernat H. K., Bodiselitsch B., 2003, *International Journal of Astrobiology*, **2**, 195
- Leblanc F., et al., 2017, *Journal of Geophysical Research: Planets*, **122**, 2401
- Leblanc F., et al., 2019, *Geophys. Res. Lett.*, **46**, 4144
- Lee Y., Combi M. R., Tenishev V., Bougher S. W., Deighan J., Schneider N. M., McClintock W. E., Jakosky B. M., 2015a, *Geophysical Research Letters*, **42**, 9015
- Lee Y., Combi M. R., Tenishev V., Bougher S. W., Lillis R. J., 2015b, *J. Geophys. Res.*, **120**, 1880
- Lewkow N. R., Kharchenko V., 2014, *ApJ*, **790**, 98
- Li B., Han K.-L., 2009, *Journal of Physical Chemistry A*, **113**, 10189
- Lillis R. J., et al., 2015, *Space Sci. Rev.*, **195**, 357
- Lillis R. J., et al., 2017, *Journal of Geophysical Research: Space Physics*, **122**, 3815
- Liu S. C., Donahue T. M., 1975, *Icarus*, **24**, 148
- Liu S. C., Donahue T. M., 1976, *Icarus*, **28**, 231
- Maiti B., Schatz G. C., 2003, *J. Chem. Phys.*, **119**, 12360
- Manolopoulos D. E., 1986, *J. Chem. Phys.*, **85**, 6425
- McGuire P., Kouri D. J., 1974, *J. Chem. Phys.*, **60**, 2488
- Mullaney Harvey N., 1982, *Chemical Physics Letters*, **88**, 553
- Nagy A. F., Cravens T. E., 1988, *Geophysical Research Letters*, **15**, 433
- Peterson K. A., Adler T. B., Werner H.-J., 2008, *J. Chem. Phys.*, **128**, 084102
- Rahmati A., et al., 2018, *Journal of Geophysical Research (Planets)*, **123**, 1192
- Schatz G. C., Redmon M. J., 1981, *Chemical Physics*, **58**, 195
- Sharma R. D., Wintersteiner P. P., 1990, *Geophysical Research Letters*, **17**, 2201
- Shematovich V. I., 2017, *Solar System Research*, **51**, 249
- Sun C., Shao X., Yu C., Feng E., Huang W., 2012, *Chemical Physics Letters*, **549**, 12
- Suzukawa Jr H. H., Wolfsberg M., Thompson D. L., 1978, *J. Chem. Phys.*, **68**, 455
- Thiemens M. H., Jackson T. L., Brennkmeijer C. A., 1995, *Geophysical Research Letters*, **22**, 255
- Thiemens M. H., Chakraborty S., Jackson T. L., 2014, *Journal of Geophysical Research: Atmospheres*, **119**, 6221
- Upschulte B. L., Caledonia G. E., 1992, *J. Chem. Phys.*, **96**, 2025
- Uudus N., Magaki S., Balakrishnan N., 2005, *J. Chem. Phys.*, **122**, 024304
- Werner H.-J., Adler T. B., Knizia G., Manby F. R., 2010, in *Recent Progress in Coupled Cluster Methods*. Springer, pp 573–619
- Werner H.-J., Knizia G., Manby F. R., 2011, *Molecular Physics*, **109**, 407
- Werner H.-J., et al., 2012a, MOLPRO, version 2012.1, a package of ab initio programs
- Werner H.-J., Knowles P. J., Knizia G., Manby F. R., Schütz M., 2012b, *WIREs Computational Molecular Science*, **2**, 242
- Wiegel A. A., Cole A. S., Hoag K. J., Atlas E. L., Schaufler S. M., Boering K. A., 2013, *Proceedings of the National Academy of Sciences*, **110**, 17680
- Wolf A., Reiher M., Hess B. A., 2002, *J. Chem. Phys.*, **117**, 9215
- Yeung L. Y., et al., 2012, *Journal of Physical Chemistry A*, **116**, 64
- Zahnle K., Haberle R. M., Catling D. C., Kasting J. F., 2008, *Journal of Geophysical Research: Planets*, **113**, E11004
- Zhang P., Kharchenko V., Dalgarno A., Matsumi Y., Nakayama T., Takahashi K., 2008, *Physical Review Letters*, **100**, 103001
- Zhang P., Kharchenko V., Jamieson M. J., Dalgarno A., 2009, *J. Geophys. Res.*, **114**, A07101
- de Lara-Castells M. P., Hernández M. I., Delgado-Barrio G., Villarreal P., López-Puertas M., 2006, *J. Chem. Phys.*, **124**, 164302
- de Lara-Castells M. P., Hernández M. I., Delgado-Barrio G., Villarreal P., López-Puertas M., 2007, *Molecular Physics*, **105**, 1171

This paper has been typeset from a $\text{\TeX}/\text{\LaTeX}$ file prepared by the author.